CrossMark

ORIGINAL PAPER

A neutron diffraction study of crystal and low-temperature magnetic structures within the (Na,Li)FeGe$_2$O$_6$ pyroxene-type solid solution series

Günther J. Redhammer[1] · Anatoliy Senyshyn[2] · Stefan Lebernegg[3,4] · Gerold Tippelt[1] · Edgar Dachs[1] · Georg Roth[5]

Abstract Solid solution compounds along the Li$_{1-x}$Na$_x$FeGe$_2$O$_6$ clinopyroxene series have been prepared by solid state ceramic sintering and investigated by bulk magnetic and calorimetric methods; the Na-rich samples with x(Na) > 0.7 were also investigated by low-temperature neutron diffraction experiments in a temperature range of 4–20 K. For samples with x(Na) > 0.76 the crystal structure adopts the $C2/c$ symmetry at all measuring temperatures, while the samples display $P2_1/c$ symmetry for smaller Na contents. Magnetic ordering is observed for all samples below 20 K with a slight decrease of T_N with increasing Na content. The magnetic spin structures change distinctly as a function of chemical composition: up to x(Na) = 0.72 the magnetic structure can be described by a commensurate arrangement of magnetic spins with propagation vector $\mathbf{k}$ = (½, 0 0),

an antiferromagnetic (AFM) coupling within the Fe^{3+}O$_6$ octahedra zig-zag chains and an alternating AFM and ferromagnetic (FM) interaction between the chains, depending on the nature of the tetrahedral GeO$_4$ chains. The magnetic structure can be described in magnetic space group P_a2_1/c. Close to the structural phase transition for sample with x(Na) = 0.75, magnetic ordering is observed below 15 K; however, it becomes incommensurately modulated with $\mathbf{k}$ = (0.344, 0, 0.063). At 4 K, the magnetic spin structure best can be described by a cycloidal arrangement within the M1 chains, the spins are within the **a**–**c** plane. Around 12 K the cycloidal structure transforms to a spin density wave (SDW) structure. For the $C2/c$ structures, a coexistence of a simple collinear and an incommensurately modulated structure is observed down to lowest temperatures. For 0.78 ≤ x(Na) ≤ 0.82, a collinear magnetic structure with $\mathbf{k}$ = (0 1 0), space group P_C2_1/c and an AFM spin structure within the M1 chains and an FM one between the spins is dominating, while the incommensurately modulated structure becomes dominating the collinear one in the samples with x(Na) = 0.88. Here the magnetic propagation vector is $\mathbf{k}$ = (0.28, 1, 0.07) and the spin structure corresponds again to a cycloidal structure within the M1 chains. As for the other samples, a transition from the cycloidal to a SDW structure is observed. Based on the neutron diffraction data, the appearance of two peaks in the heat capacity of Na-rich samples can now be interpreted as a transition from a cycloidal magnetic structure to a spin density wave structure of the magnetically ordered phase for the Na-rich part of the solid solution series.

✉ Günther J. Redhammer
guenther.redhammer@sbg.ac.at

1 Chemistry and Physics of Materials, Division Materials Science and Mineralogy, University of Salzburg, Jakob-Haringerstrasse 2A, 5020 Salzburg, Austria

2 Heinz Maier-Leibnitz-Zentrum (MLZ), Technische Universität München, Lichtenbergstrasse 1, 85747 Garching, Germany

3 Leibniz Institute for Solid State and Materials Research, 01171 Dresden, Germany

4 Max Planck Institute for Chemical Physics of Solids, Nöthnitzer Str. 40, 01187 Dresden, Germany

5 Institute of Crystallography, RWTH Aachen University, Jägerstraße 17/19, 52056 Aachen, Germany

Springer

Introduction

Minerals of the pyroxene family are important constituents of Earth crust and Earth mantle and have both a rich crystal- and a rich magneto-chemistry. As complex magnetic systems, the pyroxenes have attracted vivid interest because of their intriguing low-dimensional magnetic and multi-ferroic properties (Ackermann et al. 2015; Jodlauk et al. 2007). Owing to their chemical flexibility, the pyroxene-type compounds offer an enormous and fancy playground to study the various magnetic properties as a function of composition by tuning magnetic exchange pathways with chemical substitutions. This relation between chemical composition, crystal structure (symmetry) and magnetic properties is a main issue of the present work. Besides magnetic phase transitions, especially the Li-bearing clinopyroxenes show crystallographic phase transitions from a low-temperature $P2_1/c$ to a high-temperature $C2/c$ structure (Alvaro et al. 2011; Camara et al. 2009; Nestola et al. 2009; Redhammer et al. 2010a; Redhammer and Roth 2004a, b; Redhammer et al. 2001, 2015; Tribaudino et al. 2002, 2003). Analogue Na- pyroxenes, however, retain the $C2/c$ structure down to lowest temperatures (Redhammer and Tippelt 2014). Key features in both, the $P2_1/c$ and the $C2/c$ structures, are infinite edge-sharing zig-zag chains of octahedrally coordinated M1-sites hosting Fe^{3+}. These chains are separated by infinite chains of corner—sharing GeO_4 tetrahedra. Main differences between the two structure-types are changes in the geometry of the transition metal bearing M1 site, in the M2 (Na, Li) site geometry and—most important—two independent tetrahedral chains in the $P2_1/c$ structure, often denoted as A and B chains, as compared to one symmetrically identical tetrahedral chain in $C2/c$. This allows additional different magnetic interaction pathways in $P2_1/c$. Most of the "magnetic pyroxenes" order in a rather simple way below T ~40 K, from fully ferromagnetic to fully antiferromagnetic within and between the M1 chains (Cheng et al. 2013; Janson et al. 2014; Nenert et al. 2009b, 2010b; Redhammer et al. 2008, 2009, 2010b, 2011b, 2012, 2013, 2015). Only a few compounds are reported exhibiting a complex cycloidal magnetic ordering, among them $NaFeGe_2O_6$ and $NaFeSi_2O_6$ (Drokina et al. 2011; Redhammer et al. 2011a). These two compounds feature a dielectric polarization and were proven to be multi-ferroic materials (Jodlauk et al. 2007; Kim et al. 2012). Generally, materials with helical/cycloidal ordering were recognized as potential multiferroics (e.g. Park et al. 2007). Such multiferroics, materials, which are simultaneously (ferro)magnetic, ferro-electric and partly also ferro-elastic, considerably attract attention due to the interesting physics involved and the promising practical applications (Dong et al. 2015; Fiebig et al. 2016; Jodlauk et al. 2007; Khomskii 2006, 2014; Spaldin and Fiebig 2005; Tokura 2006).

Different pathways for magnetic super-exchange are possible in the pyroxene structure (see also Fig. 6): J_1 runs within the M1 chain, J_2 is a super–super-exchange between M1 atoms in two different M1 chains with the smallest distance (~5.3–5.8 Å) involving the tetrahedral sites. For the $P2_1/c$ symmetry with two different tetrahedral chains, also two slightly different J_2 paths exist. J_3 is another inter-chain coupling path, which involves more distant (7–8 Å) M1 sites in different chains, leading to a triangular configuration. Competing exchange interactions, i.e. magnetic frustrations, within and between the M1 chains are responsible for the quite diverse magnetic ground states even in (chemically) very similar systems. In several papers on pyroxenes, it was shown that the magnetic spin structures depend in a delicate way on small structural changes, e.g. (Janson et al. 2014; Nenert et al. 2010a; Redhammer et al. 2013; Streltsov and Khomskii, 2008). This relation has extensively been studied, particularly for spin-1/2 systems like Cu^{2+} compounds. Lebernegg et al. (2017), e.g. pointed out that in spin-1/2 chains a complex interplay of quantum fluctuations, exchange interactions and lattice topologies are responsible for rich magnetic phase diagrams and often result in magnetic frustration. The relation between strengths of nearest-neighbour and next-nearest-neighbour interaction within and between such chains, structural details and covalency are keys for understanding magnetic ground states (Braden et al. 1996; Furukawa et al. 2010; Geertsma and Khomskii 1996; Lebernegg et al. 2013a, b, 2014, 2016; Ruiz et al. 1997). For spin-5/2 compounds, the situation is even more complicated because of 5 instead of only one magnetic orbital per magnetic site and orbital degrees of freedom.

Investigations along solid solutions series with the same M1 cation, but different magnetic ground states and paramagnetic symmetries of the end-members, are of interest to puzzle out in more detail in which ways the chemical composition tailors the development and interchange of magnetic structures.

The crystal structures of $(Na,Li)FeGe_2O_6$ solid solution compounds were investigated in detail by Redhammer and Tippelt (2016) using single-crystal X-ray diffraction. The $P2_1/c$ structure is conserved over a wide range of compositions at 100 K. From extrapolation of available data, a change of symmetry is expected between Na contents of x(Na) ~0.85–0.90 for temperatures of about 20 K. In a very recent study of Drokina et al. (2016), the change in symmetry from $C2/c$ to $P2_1/c$ in the $Li_xNa_{1-x}FeGe_2O_6$ system in the 100 K to 800 K region, found by Redhammer and Tippelt (2016), was fully confirmed.

The magnetic structure of $P2_1/c$ $LiFeGe_2O_6$ was determined by Redhammer et al. (2009). It is commensurate with $\mathbf{k} = (½\ 0\ 0)$ with an antiferromagnetic (AFM) coupling of spins within the M1 chains, while the inter-chain coupling is ferromagnetic (FM) via the GeA-chain and AFM via the GeB-chain. This alternating FM and AFM coupling between the M1 chains is responsible for the doubling of a in the magnetic unit cell. Very recently Drokina et al. (2015) found a magnetic structure for the intermediate compound $Li_{0.5}Na_{0.5}FeGe_2O_6$ with $P2_1/c$ symmetry at low temperature and found a very similar magnetic structure to the one of the $LiFeGe_2O_6$ end-member. In contrast $NaFeGe_2O_6$ shows complex magnetic ordering with a cycloidal incommensurate ordering of spins within the M1-chains and $k = (0.323\ 1.0\ 0.080)$ (Drokina et al. 2011; Redhammer et al. 2011a). For $NaFeGe_2O_6$, Kim et al. (2012) concluded from ferro-electric measurements that the compound orders magnetically in a two-steps process. At 12 K, a transition into a para-electric AFM phase below is observed, below 10 K it features a ferro-electric AFM phase with incommensurate ordering. Similar results were provided by Ackermann et al. (2015) from dielectric, magnetic and magneto-elastic properties.

Unravelling how the transition from the commensurate magnetic structure in $LiFeGe_2O_6$ to the incommensurately modulated cycloidal one in $NaFeGe_2O_6$ as a function of Li–Na substitution takes place is the goal of the present study. For this reason, we have investigated samples of the $Li_{1-x}Na_xGe_2O_6$ series using calorimetric, bulk magnetic and neutron diffraction methods on polycrystalline samples.

Experimental

Material synthesis

For magnetometry and calorimetric measurements, sample material of the study of Redhammer and Tippelt (2016) was used. For neutron diffraction experiments, additional samples along the $Li_{1-x}Na_xFeGe_2O_6$ series with $x(Na) = 0.7–0.9$ were synthesized using a ceramic sintering route. Starting materials were prepared from stoichiometric mixtures of Na_2CO_3, Li_2CO_3, Fe_2O_3 and GeO_2, which were intimately grounded under ethanol to ensure good homogeneity. These mixtures were pressed to pellets in ~12 g batches, placed into open platinum crucibles and fired on air for one day at 1273 K in a first step for calcinations. Afterwards the pellets were reground, pressed again and fired at 1273 K for additional 5 days. To ensure complete reaction, phase purity and good crystallinity, this procedure was repeated three times.

Samples prepared as described were pale green-brown to brown in colour and showed crystal sizes up to 10 μm.

Neutron diffraction experiments

Neutron diffraction experiments were done at the Maier-Leibnitz-Zentrum (MLZ), FRM-II, Munich, Germany. Powder diffraction data were acquired between 4 and 20 K in constant wavelength mode using the high-resolution powder diffractometer SPODI (Hoelzel et al. 2012) on ~10 g batch with Ge331 monochromatized neutron radiation ($\lambda = 2.5360$ Å). Experiments were performed in a 2θ range $3° \leq 2\theta \leq 154°$, step width 0.04° using a closed cycle cryostat with the sample contained in a V-can. High data acquisition time of 2.5 h was used for 4 and 20 K data, while 0.5 h runs were used to scan the variation of magnetic moments and phase transitions within a tight temperature grid. Data treatment was performed using the FullProf Suite of programs (Rodríguez-Carvajal, 2001). The structural data of (Redhammer and Tippelt, 2016) were taken as starting parameters in Rietveld refinements. During refinements, we became aware of very small amounts of hematite, which are <0.3 wt%, but detectable in the neutron diffraction data, while not in the X-ray powder diffraction data. The magnetic symmetry analysis was performed with the module MAXMAGN (Perez-Mato et al. 2015) as provided by the Bilbao Crystallographic server http://www.cryst.ehu.es/ (Aroyo et al. 2006a, b, 2011).

Low-temperature calorimetric measurements

Low-temperature heat capacities were measured using a commercially designed relaxation calorimeter (the heat capacity option of the Quantum Design PPMS) at Salzburg University. The data were collected in triplicate between 2 and 300 K, using a logarithmic spacing. Further details will be given in a separate paper on the thermodynamic $P2_1/c − C2/c$ phase transition and mixing properties of the (Li,Na)FeGe_2O_6 solid solution (Dachs et al. in prep).

Bulk magnetic measurements

The magnetization was measured at the MPI CPfS in Dresden, using a Quantum Design (QD) SQUID MPMS in static fields up to 5 T in the temperature range of 2.0–400 K. Measurements up to 7 T were performed with a vibrating sample magnetometer (VSM) setup of the QD PPMS. The masses of the powder samples were between 15 and 20 mg. Owing to the presence of the very small amounts of hematite, we carefully looked for any signature of hematite in the magnetization data, but, did not find any.

The field dependence of the magnetic susceptibility is linear at low fields and perfectly intercepts zero.

Results and discussion

SQUID magnetic susceptibility measurements

The temperature-dependent magnetic susceptibility $\chi(T)$ of the $Li_{1-x}Na_xFeGe_2O_6$ compounds was measured in magnetic fields of 0.05, 0.5, 5 T. The lowest field was applied to scan for possible small additional features in $\chi(T)$, which, however, could not be detected in any of the presented compounds. Owing to the stronger noise at very low fields, only data collected at 0.5 and 5 T are shown in the plots (Fig. 1). All compounds feature a maximum in $\chi(T)$ in the temperature range 25–35 K which shifts to higher temperatures and broadens with increasing Na content. As outlined in detail by Redhammer et al. (2011a), pure $NaFeGe_2O_6$ has the largest difference between T_{max} and T_N in the susceptibility data and exhibits the broadest maximum. With increasing Li content, the maximum becomes "sharper" and the difference between T_{max} and T_N smaller. This is interpreted as a distinct quasi 1D behaviour in $NaFeGe_2O_6$; as interatomic bond lengths and angles stay rather constant within the M1 chain, while the chain to chain separation increases, we assume this effect to be mainly due to a decrease in J_2. However, frustration may considerably compromise such conclusions. Without calculating the exchanges or having an experimental value, it is difficult to give a more in-depth conclusion.

Below the maximum, a kink in $\chi(T)$ is visible that can be attributed to magnetic ordering. Below this transition, the susceptibility data collected at a magnetic field of 0.5T are lower than that measured at 5T, evidencing a spin-flop transition. This transition is also visible in field-dependent magnetization data $M(H)$ as a slight change of the slope in the field regime of 1.4–4T. The minimum field is observed for $x(Na) = 0.75$ in agreement with the lowest ordering temperature determined from $\chi(T)$ (see below). In most datasets, $\chi(T)$ features an upturn below the magnetic transition which is more pronounced at higher magnetic fields. The magnetic field should actually suppress paramagnetic contributions whose Curie-behaviour can be responsible for such an upturn. Therefore, we expect that it is actually an intrinsic effect. This is supported by the fact that the upturn is very small for $H = 0.5$ T and even missing in the $x(Na) > 0.8$ compounds.

The magnetic ordering temperature was estimated from the position of the maximum in the magnetic contribution $C_{mag}(T)$ to the specific heat $C_p(T)$. $C_{mag}(T)$ was determined from the susceptibility data by using the Fisher relation $d(\chi(T)T)/dT \sim C_{mag}(T)$ (Fisher 1962). The results are provided in Table 1 and Fig. 2 which also show data of Drokina et al. (2016). T_N decreases with increasing Na content up to $x(Na) = 0.75$. In between $x(Na) = 0.75$ and $x(Na) = 0.80$, T_N jumps up by about 3 K and then decreases smoothly

Fig. 1 Selected magnetic susceptibility measurements for samples of the $Li_{1-x}Na_xFeGe_2O_6$ solid solution series
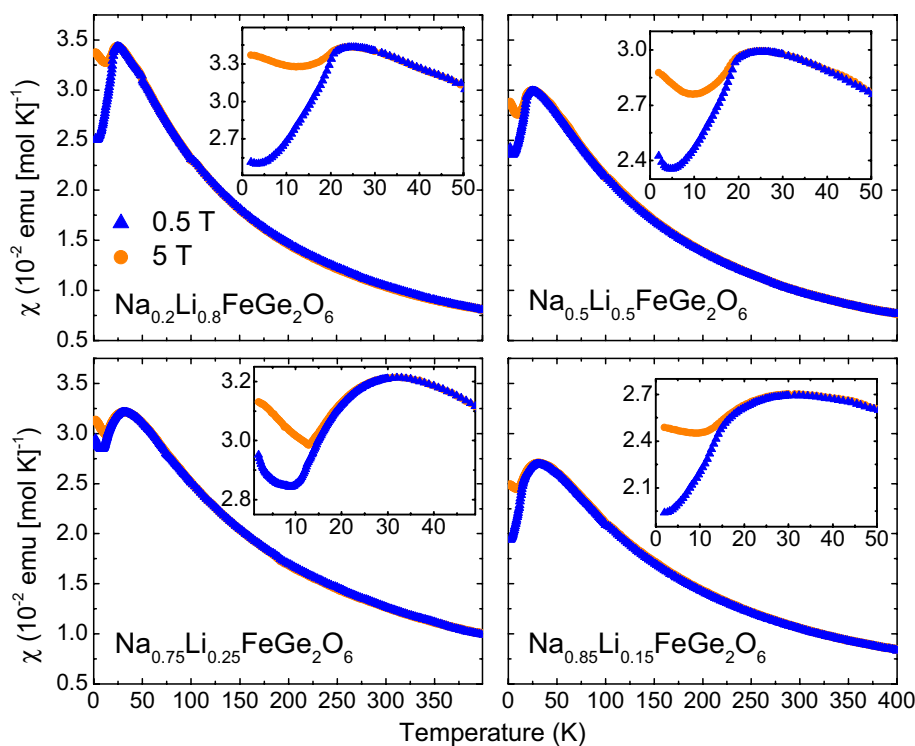
Table 1 Results of magnetic peak position determination in caloric measurements and evaluation of bulk magnetic measurements (neel temperature T_N, paramagnetic Curie temperature) as a function of the Na content of the polycrystalline samples along the $Li_{1-x}Na_xFeGe_2O_6$ solid solution series

X(Na)	C_p Peak 1	C_p Peak 2	T_N (K)	T_N (K)[a]	Θ_p (K)[b]	Θ_p (K)[a]	J/k[c]	G[c]
0	20.2		20.2					
0.1	20.7			17.5		−50		
0.2	20.4		20	19	65	−75	7.17	1.75
0.3	20.5							
0.4	19.8							
0.5	19.0		18.8	18	48	−14	7.7	1.7
0.6	17.8		17.4		72		8.11	1.68
0.7	15.0		14.2	13.1	58	−107	8.86	1.73
0.75	14.9	13.3	12		74		8.75	1.86
0.8	14.9	12.3	15		75		9.19	1.81
0.85	14.3	12.2	14.2		101		8.81	1.72
0.9	13.9	12.0	13.5	11.9	101	−125	9.91	1.8
1	13.2	11.8	11.2	13		−135		

[a] Data of Drokina et al. (2016)

[b] A positive sign means AFM coupling here with the Hamiltonian used for witting the data

[c] Estimation of the inter-chain coupling using the Bonner–Fisher model
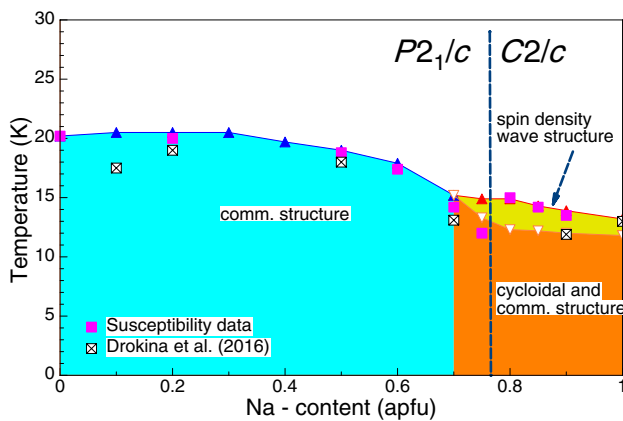
Fig. 2 *T–X* phase diagram showing magnetic ordering temperatures as determined by bulk magnetization and calorimetric methods for samples of the $Li_{1-x}Na_xFeGe_2O_6$ series. *Filled* and *open triangles* are the C_p data (1st and 2nd peak), the data of Drokina et al. (2016) are included for comparison, the kind of magnetic structure indicated is determined from neutron diffraction (see below), the *dashed vertical line* is the estimated phase boundary between *P2₁/c* (*left*) and *C2/c* (*right*) crystal structure, a full paramagnetic structural phase diagram is given in the ESM Figure S2 (comm. means commensurate)

again. For $x(Na) = 0.85$, the peak in $d(\chi(T)T)/dT$ becomes broader and at $x(Na) = 0.90$ a double-peak structure appears (see Electronic Supplementary Material (ESM) Figure S1). This double peak is also seen in the $C_p(T)$ measurements (see below). Its appearance in $d(\chi(T)T)/dT$ demonstrates that both peaks come from magnetic transitions.

From earlier work on Li and Na Ge-pyroxenes (Redhammer et al. 2009, 2011a), it is known that the Li and Na end-members of this solid solution have different magnetic structures. However, it was not clear how they transform into each other. Since T_N remains above 12 K for all compounds (Table 1), we can exclude that the commensurate structure of the Li-compound is suppressed before the incommensurate structure of the Na-compound appears. Rather they transform into each other continuously.

We also performed a Curie–Weiss fit of $1/\chi(T)$ for the temperature range of 320–395 K. $1/\chi(T)$ actually seems to follow a linear behaviour already at much lower temperatures but no stable fit could be obtained at lower temperatures, owing to very small non-linearities. This is in agreement with the paramagnetic Curie temperatures Θ_P ranging from 50 to 100 K, suggesting the presence of antiferromagnetic couplings of sizable strength. It should be noted here that with our definition of the Hamiltonian, a positive sign of Θ_P means antiferromagnetic coupling! The magnetic moments are in between 5.4 and 6.4 μ_B/Fe^{3+}. In contrast to T_N, none of the parameters obtained with the Curie–Weiss fits show a clear smooth trend with respect to the Na content of the samples (see Table 1). Nevertheless, the paramagnetic Curie temperature suggests strong overall antiferromagnetic (AFM) coupling in the $Li_{1-x}Na_xFeGe_2O_6$ compounds. There is a small tendency of a decreasing Θ_P indicative of a decreasing overall AFM character of the samples toward the $LiFeGe_2O_6$ end-member. We also applied an estimation of the intra-chain coupling by fitting the susceptibility data with the Bonner–Fischer model. Fitting data are included in Table 1. In line with the observations of Redhammer et al. (2011a), the data show—at least semi-quantitatively—that in $NaFeGe_2O_6$ the intra-chain coupling constant is largest, while with increasing Li content J/k decreases. As can be followed from the data, Na-rich samples display a more distinct low-dimensional behaviour, with a weak inter-chain coupling. These

observations are in perfect agreement with the magnetic spin structures found below.

Calorimetric data

The low-temperature calorimetric data of $Li_{1-x}Na_xFeGe_2O_6$ compounds confirm magnetic ordering at low temperatures, which is evident by the appearance of a clear detectable λ-peak in the heat capacity C_p (Fig. 3). Pure $LiFeGe_2O_6$ orders magnetically at 20.2 K in good agreement with the data reported by Redhammer et al. (2009). Increasing the Na content does not alter the ordering temperature significantly up to x(Na) ~0.3 as can be inferred from Fig. 2; for higher Na contents, the magnetic ordering temperature decreases almost linearly down to 13.2 K in the Na- end-member. The heat capacity measurements clearly give evidence for two peaks in the end-member composition $NaFeGe_2O_6$, the first one at 13.2 K, the second at 11.9 K. The appearance of two peaks in C_p of $NaFeGe_2O_6$ was first noticed by Drokina et al. (2011) and assigned to a change
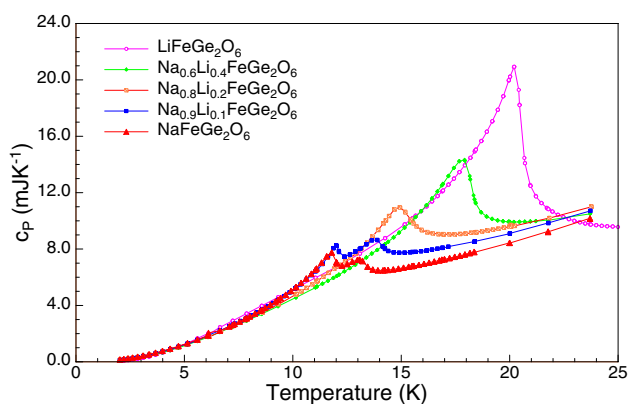
in the macroscopic state of the magnetic subsystem. Similarly, two peaks are also observed for $Li_{0.1}Na_{0.9}FeGe_2O_6$ with maxima at 13.9 and 12.0 K. For the samples with x(Na) = 0.75 and 0.90, the high-temperature peak is well resolved, while the second one is only visible as an ill-defined shoulder, for x(Na) = 0.75 two peaks can readily be resolved, while for samples with x(Na) < 0.75 only one peak is found. The appearance of two peaks in C_p is seen as an evidence for two magnetic phase transitions in the Na-rich compositions. An in-depth investigation of the *thermodynamic properties* of the $Li_{1-x}Na_xGe_2O_6$ solid solution series goes beyond the scope of this contribution and will be given elsewhere in a subsequent work (Dachs et al. in prep.).

Low-temperature neutron diffraction

Nuclear structure at 20 K

The neutron diffraction data were collected for nominal compositions $Li_{1-x}Na_xFeGe_2O_6$ with x(Na) = 0.9, 0.85, 0.80, 0.75 and 0.70. All powder diffraction data could be refined to low R-values for all samples and temperatures, the results for the 20 K measurements in the paramagnetic state are given in Tables 2, 3, 4, data for the 4 K measurements are compiled in the ESM Table S1, while lattice parameters and magnetic moments for all other samples and temperatures are summarized in ESM Table S2. The distinct difference in neutron cross section between Na and Li allowed for a good determination of the amount of Na and Li on crystallographic M2 sites, thus the effective substitutional rate within the samples prepared for neutron diffraction experiments can be determined. The obtained Na/Li distribution agrees well with the nominal stoichiometry with a small surplus of Li (see Table 2). Detailed analysis of the diffraction data at 20 K showed that samples with x(Na) > 0.78 display $C2/c$ symmetry, while these with x(Na) $\leq$ 0.75 already have $P2_1/c$ symmetry. The change in

Fig. 3 Low-temperature heat capacity for some selected compositions of the $Li_{1-x}Na_xGe_2O_6$ solid solution series, for x(Na) = 0.9 and 1.0, two peaks are evident, indicative of two magnetic phase transitions

Table 2 Experimental details and results of Rietveld refinements on constant wavelength neutron diffraction pattern ($\lambda = 2.5360$ Å) for synthetic $Li_{1-x}Na_xFeGe_2O_6$ pyroxene-type compounds at $T = 20$ K

ID	NLFGO10	NLFGO15	NLFGO20	NLFGO25	NLFGO30
x(Na)*	0.878	0.820	0.784	0.754	0.690
S.G.	$C2/c$	$C2/c$	$C2/c$	$P2_1/c$	$P2_1/c$
a (Å)	9.9968 (3)	9.9996 (3)	10.0018 (3)	9.9874 (3)	9.9837 (3)
b (Å)	8.8827 (3)	8.8891 (3)	8.8935 (3)	8.8675 (2)	8.8654 (3)
c (Å)	5.5142 (2)	5.5180 (2)	5.5203 (2)	5.5059	5.5016 (2)
$\beta°$	107.938 (5)	108.114 (5)	108.271 (4)	108.250 (5)	108.281 (5)
V (Å^3)	465.84	466.17	466.28	463.10	462.37
R_p (%)	2.83	3.03	4.05	2.86	3.05
R_{wp} (%)	3.65	3.92	5.59	3.47	3.82
R_{exp} (%)	2.00	1.99	2.15	2.08	1.98
R_{Bragg}	2.01	2.26	2.31	1.52	2.46

Table 3 Fractional atomic coordinates and isotropic atomic displacement factors for Na-rich samples of the $Li_{1-x}Na_xFeGe_2O_6$ series at 20 K, determined from Rietveld refinements on constant wavelength neutron diffraction pattern

Name	X	Y	Z	B	Occ.
$Li_{0.12}Na_{0.88}FeGe_2O_6$, 20 K					
Na1	0	0.3001 (5)	0.25	1.00 (16)	0.878 (6)
Li1	0	0.3001 (5)	0.25	1.00 (16)	0.122 (6)
Fe1	0	0.90387 (12)	0.25	0.43 (3)	1
Ge1	0.28865 (8)	0.09370 (10)	0.23153 (15)	0.53 (3)	1
O1	0.10588 (10)	0.08102 (15)	0.1323 (2)	0.69 (3)	1
O2	0.35633 (13)	0.27250 (13)	0.2976 (2)	0.97 (3)	1
O3	0.36201 (14)	0.00350 (11)	1.0215 (3)	0.67 (3)	1
$Li_{0.18}Na_{0.82}FeGe_2O_6$, 20 K					
Na1	0	0.3003 (5)	0.25	0.66 (19)	0.820 (6)
Li1	0	0.3003 (5)	0.25	0.66 (19)	0.180 (6)
Fe1	0	0.90415 (13)	0.25	0.40 (4)	1
Ge1	0.28860 (9)	0.09364 (10)	0.23280 (15)	0.42 (3)	1
O1	0.10557 (12)	0.08169 (16)	0.1323 (2)	0.68 (3)	1
O2	0.35669 (13)	0.27280 (13)	0.2969 (3)	0.82 (4)	1
O3	0.36230 (15)	0.00151 (12)	1.0258 (3)	0.80 (3)	1
$Li_{0.22}Na_{0.78}FeGe_2O_6$, 20 K					
Na1	0	0.3019 (9)	0.25	1.10 (18)	0.784 (8)
Li1	0	0.3019 (9)	0.25	1.10 (18)	0.216 (8)
Fe1	0	0.9044 (2)	0.25	0.45 (5)	1
Ge1	0.28897 (13)	0.09371 (15)	0.2342 (2)	0.52 (4)	1
O1	0.10576 (17)	0.0818 (2)	0.1334 (3)	0.84 (5)	1
O2	0.3572 (2)	0.2741 (2)	0.2967 (4)	1.04 (5)	1
O3	0.3622 (2)	0.00045 (19)	1.0303 (5)	1.05 (5)	1
$Li_{0.24}Na_{0.76}FeGe_2O_6$, 20 K					
Na	0.2550 (17)	0.4467 (6)	0.731 (2)	1.3 (2)	0.754 (6)
Li	0.25502 (17)	0.4467 (6)	0.732 (2)	1.3 (2)	0.246 (6)
Fe	0.2504 (5)	0.65389 (13)	0.24167) (	0.45 (4)	1
GeA	0.0385 (4)	0.3442 (3)	0.2421 (5)	0.35 (7)	1
GeB	0.5409 (4)	0.8432 (3)	0.2309 (5)	0.34 (7)	1
O1A	−0.1458 (5)	0.3331 (5)	0.1434 (9)	0.55 (9)	1
O2A	0.1082 (5)	0.5233 (5)	0.2890 (7)	0.74 (7)	1
O3A	0.1125 (4)	0.2606 (3)	0.5469 (6)	0.64 (7)	1
O1B	0.3578 (6)	0.8302 (5)	0.1243 (9)	0.95 (9)	1
O2B	0.6096 (5)	1.0212 (5)	0.3153 (7)	0.98 (7)	1
O3B	0.6130 (5)	0.7345 (4)	0.5084 (7)	1.26 (7)	1
$Li_{0.31}Na_{0.69}FeGe_2O_6$, 20 K					
Na	0.2596 (14)	0.4438 (6)	0.729 (2)	1.3 (3)	0.69 (1)
Li	0.2596 (14)	0.4438 (6)	0.729 (2)	1.3 (3)	0.31 (1)
Fe	0.2516 (5)	0.65360 (14)	0.2426 (6)	1.04 (4)	1
GeA	0.0393 (3)	0.3442 (3)	0.2445 (5)	1.14 (7)	1
GeB	0.5404 (3)	0.8430 (3)	0.2306 (4)	1.07 (7)	1
O1A	−0.1443 (5)	0.3358 (5)	0.1463 (8)	1.14 (9)	1
O2A	0.1076 (5)	0.5229 (4)	0.2882 (7)	1.35 (14)	1
O3A	0.1120 (4)	0.2614 (3)	0.5478 (6)	0.74 (11)	1
O1B	0.3575 (5)	0.8283 (5)	0.1226 (8)	1.42 (9)	1
O2B	0.6085 (5)	1.0198 (5)	0.3175 (7)	2.25 (13)	1
O3B	0.6136 (5)	0.7304 (4)	0.5058 (7)	2.54 (14)	1

Table 4 Selected bond lengths and angles for Na-rich samples of the $Li_{1-x}Na_xFeGe_2O_6$ series at 20 K, determined from Rietveld refinements on constant wavelength neutron diffraction pattern

X (Na)	0.88	0.82	0.78	0.76	0.69	ID
M2–O1	2.398 (4)	2.393 (4)	2.402 (7)	2.434 (13)	2.472 (11)	M2–O1A
M2–O1	2.398 (4)	2.393 (4)	2.402 (7)	2.387 (13)	2.396 (10)	M2–O1B
M2–O2	2.5480 (15)	2.5490 (18)	2.552 (3)	2.523 (15)	2.524 (10)	M2–O2A
M2–O2	2.5480 (15)	2.5490 (18)	2.552 (3)	2.514 (14)	2.521 (10)	M2–O2B
M2–O3	2.384 (4)	2.357 (4)	2.328 (6)	2.209 (11)	2.204 (9)	M2–O3A
M2–O3	2.384 (4)	2.357 (4)	2.328 (6)	2.478 (10)	2.480 (9)	M2–O3B
M2–O3	2.909 (3)	2.934 (3)	2.950 (5)	2.677 (16)	2.585 (13)	M2–O3B
M2–O3	2.909 (3)	2.934 (3)	2.950 (5)	–	–	–
Fe–O2	1.9304 (15)	1.9260 (16)	1.916 (2)	1.913 (7)	1.923 (6)	Fe–O2A
Fe–O2	1.9304 (15)	1.9260 (16)	1.916 (2)	1.927 (7)	1.938 (7)	Fe–O2B
Fe–O1	2.0513 (10)	2.0483 (10)	2.0512 (15)	2.052 (6)	2.073 (5)	Fe–O1A
Fe–O1	2.0513 (10)	2.0483 (10)	2.0512 (15)	2.048 (6)	2.032 (5)	Fe–O1B
Fe–O1	2.1073 (16)	2.1081 (17)	2.106 (2)	2.109 (6)	2.131 (6)	Fe–O1A
Fe–O1	2.1073 (16)	2.1081 (17)	2.106 (3)	2.108 (7)	2.095 (6)	Fe–O1B
Ge–O1	1.7448 (19)	1.7428 (14)	1.743 (2)	1.751 (6)	1.742 (6)	GeA–O1A
Ge–O2	1.7208 (15)	1.7222 (15)	1.730 (2)	1.721 (5)	1.713 (5)	GeA–O2A
Ge–O3	1.7420 (13)	1.7434 (20)	1.733 (2)	1.750 (5)	1.751 (5)	GeA–O3A
Ge–O3	1.7657 (16)	1.7689 (16)	1.776 (3)	1.771 (4)	1.758 (4)	GeA–O3A
	–	–	–	1.725 (5)	1.716 (5)	GeB–O2B
	–	–	–	1.742 (7)	1.739 (6)	GeB–O1B
	–	–	–	1.745 (6)	1.748 (6)	GeB–O3B
	–	–	–	1.759 (4)	1.769 (4)	GeB–O3B
Fe–Fe	3.243 (1)	3.241 (1)	3.239 (1)	3.238 (1)	3.239 (1)	Fe–Fe
Fe–Fe (A)	5.619 (1)	5.614 (1)	5.609 (1)	5.614 (1)	5.601 (1)	Fe–Fe (A)
Fe–Fe (B)	–	–	–	5.587 (1)	5.588 (1)	Fe–Fe (B)
Fe–O1A–Fe	102.39 (8)	102.48 (9)	102.36 (8)	102.36 (12)	100.77 (12)	Fe–O1A–Fe
Fe–O1B–Fe	–	–	–	102.20 (12)	103.38 (12)	Fe–O1B–Fe
Kink A	177.42 (9)	179.89 (9)	179.67 (8)	172.19 (12)	171.59 (12)	Kink A
Kink B				168.60 (12)	165.61 (12)	Kink B
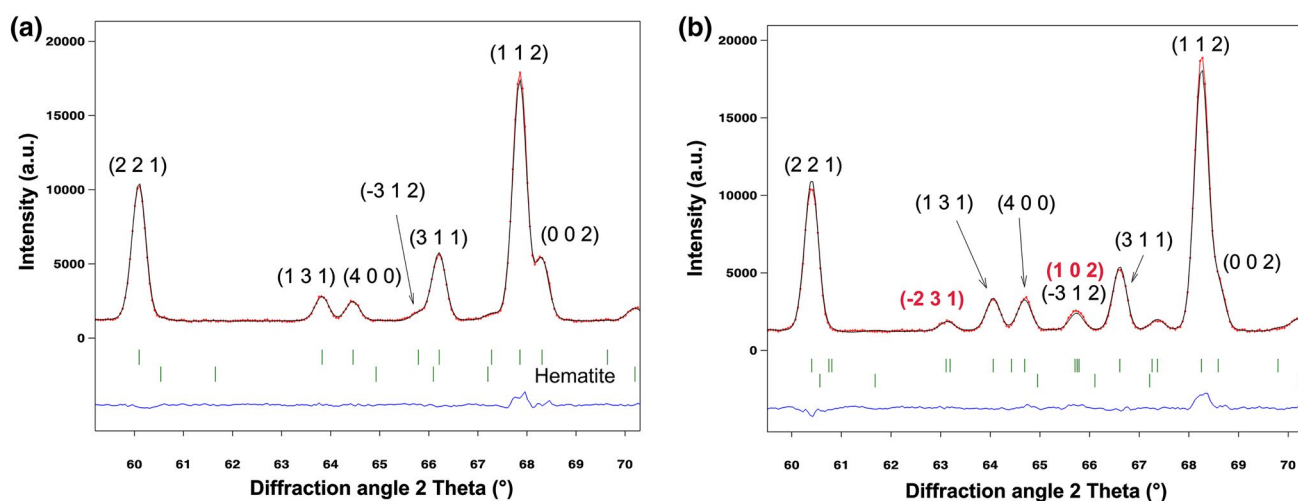
Fig. 4 Refined neutron powder diffraction data ($\lambda = 2.536$ Å) of sample $Li_{0.12}Na_{0.88}FeGe_2O_6$ **a** in the $C2/c$ symmetry and **b** sample $Li_{0.31}Na_{0.69}FeGe_2O_6$ in the $P2_1/c$ symmetry at 20 K, showing the appearance of C forbidden Bragg peaks $(-2,3,1)$, and $(1,0,2)$ in (**b**), while these are absent in (**a**)

symmetry most evidently is seen in the powder neutron diffraction data by the appearance of the $(-2\,3\,1)$ Bragg peak (Fig. 4) as was also outlined by Drokina et al. (2016). This peak of type $h + k = 2n + 1$ is non-overlapping with other peaks and forbidden by systematic extinctions within the *C* centred cell. Within one and the same composition, there is no change in symmetry down to lowest temperatures of 4 K, i.e. the crystallographic structure remains the same. Thus at 20 K, the change in space group symmetry takes place at x(Na) ~0.76–0.77 apfu, at lower contents as extrapolated in Redhammer and Tippelt (2016). This indicates a sharp drop of the $P2_1/c$ phase stability (as for x(Na) = 0.74, the transition temperature was determined to be 104 K, Redhammer and Tippelt 2016). However, this observation is consistent with the fact that in the heat capacity of samples with x(Na) > 0.75 no peak was observed, except the magnetic one. An extended structural phase diagram including the new data of this study and the ones of Drokina et al. (2016) is given in ESM Figure S2.

A comparison of lattice parameters at 20 K for the different compositions shows a sharp discontinuity when changing from $P2_1/c$ to $C2/c$ symmetry (Table 2 and ESM Fig. 3). The observation is very similar and in line with the one of Redhammer and Tippelt (2016) at 298 K, however shifted to higher Na contents at 20 K.

Within the $P2_1/c$ structure, the shortest Fe–Fe distance within the M1 chain is 3.239(2) Å and the Fe–O–Fe bond angles are 100.77(14)° and 103.38(11)°. Following the empirical Goodenough–Kanamori rules such superexchange angles will favour antiferromagnetic coupling. As is well described in literature, the $P2_1/c$ structure is characterized by the presence of two symmetry non-equivalent tetrahedral chains GeA and GeB, which differ mainly in the kinking angle. For sample $Li_{0.69}Na_{0.31}FeGe_2O_6$, these are 165.61(16)° and 171.59(17)° for the GeB- and GeA-chain,

respectively. The two different Ge-chains cause different inter-chain Fe–Fe distances, which are 5.601(2) Å and 5.588(2) Å via the GeA and the GeB chain, respectively. It is worth to note that in sample $Li_{0.25}Na_{0.75}FeGe_2O_6$, the differences between those bond lengths and angles, which become symmetrically equivalent upon the phase transition from $P2_1/c$ to $C2/c$, decrease significantly with respect to those in $Li_{0.69}Na_{0.31}FeGe_2O_6$. This is most evidently seen, e.g. for the Fe–O bond lengths and also for the Fe–O–Fe angles, which are entirely similar (see Table 4), evidencing that this sample has only small distortions from $C2/c$ symmetry and is close to the phase transition.

The three other samples with $0.78 \leq$ x(Na) ≤ 0.88 have $C2/c$ symmetry. Among several variations of bond lengths with the Na content (see Table 4), small elongations of the Fe–Fe distances, both within and between the M1-site chains can be seen. The Fe–O–Fe bond angle is ~ 102.4(1)°, thus favouring antiferromagnetic interaction; a notable feature also is the fact, that tetrahedral chains are almost extended, i.e. the tetrahedral kinking angle is very close to the ideal value of 180°.

Sample $Li_{0.31}Na_{0.69}FeGe_2O_6$ ($P2_1/c$)

Antiferromagnetic ordering leads to the appearance of additional Bragg reflections in the neutron powder pattern. For $Li_{0.31}Na_{0.69}FeGe_2O_6$ (the most Li-rich sample investigated here), these appear at temperatures between 15 K and 14 K. This temperature is in good agreement with the ordering temperatures, extracted from C_p and susceptibility measurements. The general appearance of the diffraction pattern is similar to the one of $LiFeGe_2O_6$ (Redhammer et al. 2009). The magnetic reflections in $Li_{0.31}Na_{0.69}FeGe_2O_6$ can be indexed with a propagation vector of $\mathbf{k} = (\frac{1}{2}, 0, 0)$, i.e. a doubling of the *a* lattice parameter is observed for the magnetic phase.
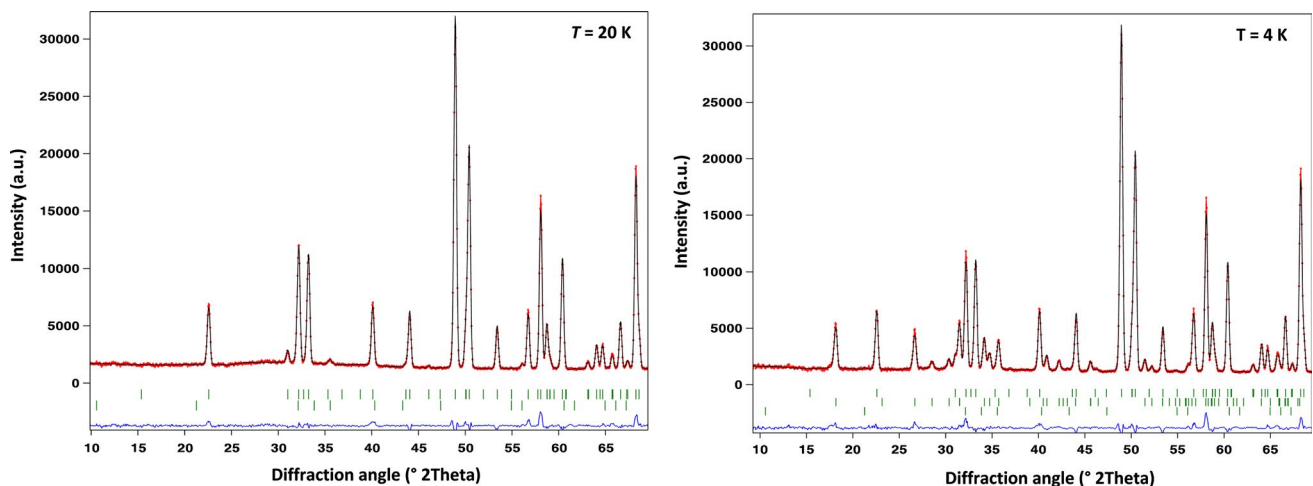

Fig. 5 Comparison between the refined neutron diffraction data ($\lambda = 2.536$ Å) at 20 and 4 K for sample $Li_{0.31}Na_{0.69}FeGe_2O_6$

Refinement of the possible magnetic structures, as determined from representational analysis and outlined in the ESM text and ESM Table S3, against the 4 K data showed that the magnetic structure of $Li_{0.31}Na_{0.69}FeGe_2O_6$ can only be given by the basis functions: $[C_x, A_y, C_z]$. Typical Rietveld refinements against the data at 4 K and 20 K are shown in Fig. 5.

$Li_{0.31}Na_{0.69}FeGe_2O_6$ possesses a magnetic structure with antiferromagnetically coupled spins within the M1 chains (Fig. 6). The appearance of AFM coupling within the M1 chains is consistent with large Fe–O–Fe angles >100° for both possible intra-chain exchange pathways in the germanate. The inter-chain coupling depends on the nature of the super-exchange pathway: $[Fe–Fe]_{inter}$ coupling via the GeA-tetrahedron is ferromagnetic. This is the longer Fe–Fe distance (5.601(2) Å) between two neighbouring Fe-chains; contrarily, the $[Fe–Fe]_{inter}$ coupling via the GeB tetrahedron is antiferromagnetic with the Fe atoms being separated by 5.588(2) Å at 4 K. The magnetic space group consistent with this ordering scheme is P_a2_1/c. This alternating FM and AFM inter-chain coupling is the reason for the doubling of the magnetic unit cell along the **a** axis. The magnetic moments are oriented along the **a** axis, with insignificant components along **b** and **c**. Also with temperature, this arrangement is not changing. The obtained magnetic structure for $Li_{0.31}Na_{0.69}FeGe_2O_6$ is consistent with the one determined by Drokina et al. (2015). Here, also the magnetic moment is aligned along the **a** axis with negligible components along **b** and **c**. However, it is different to some details to the magnetic structure of the pure Li- end-member compound. Here, the magnetic spins are aligned within the (0 1 0) plane forming an angle of ~17° with the **a** axis. The substitution of Li^+ by Na^+ obviously causes the lock in of the magnetic moments from the **a**–**c** plane to the **a** axis (Fig. 7).
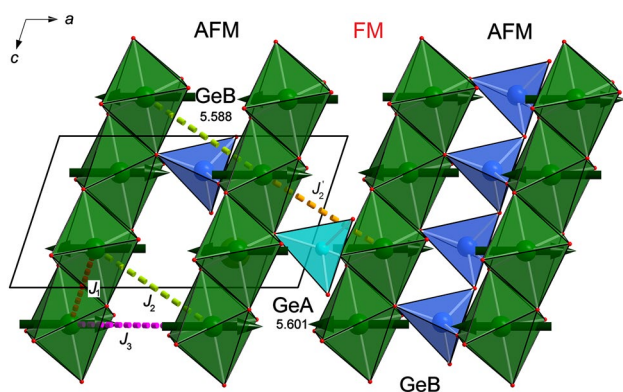

Fig. 6 Magnetic spin structure of $P2_1/c$ $Li_{0.31}Na_{0.69}FeGe_2O_6$ in a projection onto (0 1 0) at 4 K, as determined from neutron diffraction data. Note the different inter-chain couplings via GeA and GeB tetrahedral sites; J_1, J_2 and J'_2 and J_3 denote the possible pathways for magnetic super-exchange

The total magnetic moment M amounts to 3.70(6) μB at 4 K. This is a distinct reduction to the spin only value of Fe^{3+} (5.92 μB) and also is lower than the value found for $LiFeGe_2O_6$ (4.48(5) μB), and 4.30 μB for $Li_{0.5}Na_{0.5}FeGe_2O_6$ (Drokina et al. 2015). This reduction may be interpreted as increasing magnetic frustration with increasing Na^+ content and correlates well with the increasing chain separation. The variation of the magnetic moment with increasing temperature was fitted with a phenomenological power law according to

$$M(T) = M(0) \times [1 - (T - T_N)]^{\beta}, \qquad (1)$$

which forces a $M(T) \propto [1 - (T/T_N)]^{\beta}$ behaviour in the critical region near T_N while a $M(T) = M(0) \times [1 - cT^{\alpha}]$ behaviour is obtained at $T \to 0$ (Blundell et al. 2003). The fittings yield $M(0) = 3.75(1)$ μ_B, $T_N = 14.3(1)$ K, $\alpha = 2.7(2)$ and a critical exponent $\beta = 0.319(3)$; the critical exponent β is consistent with a 3D model of ordering. It should be noted that due to the low data to parameter values, the fits for all samples mainly should serve as guides to the eye, rather than give "hard" physical data. Nevertheless, the obtained data show plausible values (see also ESM Table S5).

$Li_{0.25}Na_{0.75}FeGe_2O_6$ with $P2_1/c$ symmetry

This composition also shows $P2_1/c$ symmetry down to 4 K as evidenced by the presence of the (−2 3 1) Bragg peak. This peak does not change its intensity throughout the whole temperature range. First magnetic Bragg peaks appear between 14 K and 15 K; the general appearance,
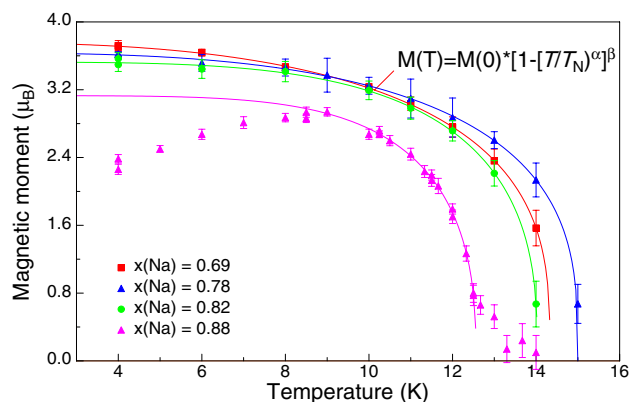

Fig. 7 Variation of the total magnetic moments in $Li_{1-x}Na_xFeGe_2O_6$ samples as a function of temperature as determined from Rietveld refinements of neutron diffraction data. The function fitted to the data is a power law with $M(T) = M(0)*[1 - (T/T_N)^{\alpha}]^{\beta}$ and should mainly serve as a guide to the eye; the decrease in M for the sample with $x(Na) = 0.88$ below 9 K is due to changing relative area fraction of the collinear magnetic structure on the extent of the modulated one (see text and ESM for details)

however, is different to $Li_{0.31}Na_{0.69}FeGe_2O_6$ (see ESM Figure S4). Any attempts to index the magnetic peaks at 4 K with a commensurate **k** vector failed, but were successful with **k** = (0.344, 0, 0.0634). With this, a magnetic structure with the spins being oriented within the (0 1 0) plane could be obtained; similar to all other samples, there is no significant magnetic moment along the **b** axis, thus in the final refinements, the magnetic moment was fixed to be aligned within the **a**–**c** plane. Within the M1 chain, there is a cycloidal arrangement of spins, the coupling along J_1 is close to antiferromagnetic while along J_2 it can take any kind of interaction, from FM to AFM, depending on the local environment (Fig. 8). Close to the $P2_1/c$ – $C2/c$ phase transition composition, the AFM coupling within the M1 chain is preserved, while the inter-chain coupling is close to magnetic frustration causing the incommensurate modulation.

Between 11 and 12 K, there is a transition from the cycloidal to a spin density wave phase. This is also seen by a change in the **k** vector, which increases significantly for $\mathbf{k}_x$, but drops for $\mathbf{k}_z$ (see ESM Figure S5). Additionally, the phase change is also visible in the neutron diffraction pattern. The SDW structure has the spins oriented almost parallel to the **a** axis with an AFM arrangement along J_1 and a FM arrangement between the M1 chains along J_2. Except the spin density wave structure, this type of coupling is the same as found for the collinear magnetic structures in the samples with $0.78 \leq x(Na) \leq 0.88$.
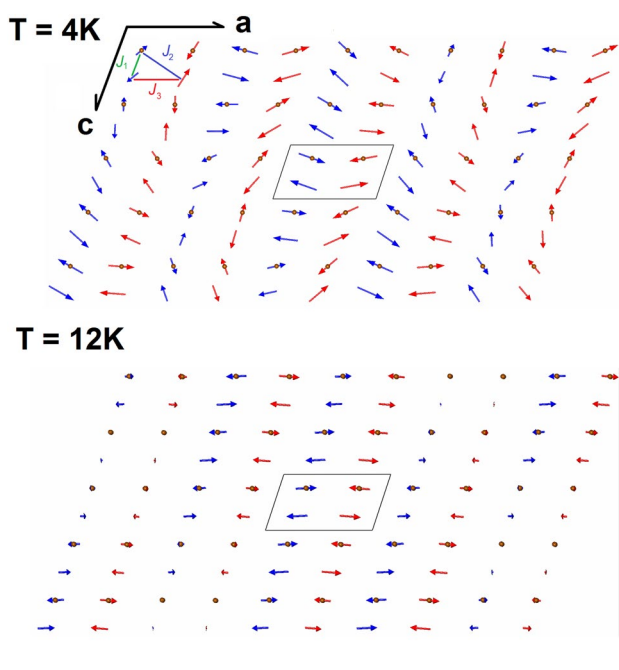
Fig. 8 Scheme of the two different magnetic structures in $Li_{0.25}Na_{0.75}FeGe_2O_6$ at low temperatures as determined from the powder neutron diffraction data

$Li_{1-x}Na_xFeGe_2O_6$ samples with C2/c symmetry (x(Na) = 0.78, 0.82. 0.88)

In the samples $Li_{0.22}Na_{0.78}FeGe_2O_6$ and $Li_{0.18}Na_{0.82}FeGe_2O_6$ first magnetic Bragg peaks appear between 15–14 and 14–13 K, respectively. The general appearance of the diffraction pattern at 4 K is very similar for both samples, but differs from the ones of the $P2_1/c$ samples described above. Main magnetic Bragg peaks at 4 K can be indexed in $C2/c$ symmetry on the basis of a commensurate propagation vector with **k** = (0 1 0), which is symmetry equivalent to **k** = (1, 0, 0) for the C centred lattice. For synthetic $NaFeSi_2O_6$, Baum et al. (2015) also determined **k** = (0 1 0), in this later paper a detailed symmetry analysis of the $C2/c$ space group is also given. The magnetic spins are coupled AFM within the M1 chains along J_1, while the coupling between the chains along the shortest Fe–Fe$_{inter}$ distance is FM (J_2). The magnetic symmetry, consistent with this ordering scheme is P_C2_1/c. The magnetic moment is oriented along the **a** direction, no significant magnetic moment component was found along **c**, both in refinements with components M_x, M_z and in those with polar angles (deviation from **a** by ± 2°). The magnetic structure of the two compounds with x(Na) = 0.78 and 0.82 correlates with the collinear AFM and FM coupling subsystem via the GeA tetrahedra in $P2_1/c$ $Li_{1-x}Na_xFeGe_2O_6$ samples. However, this arrangement is unique to some extent, as it was observed so far only for clinopyroxenes with $P2_1/c$ symmetry, e.g. for $LiVGe_2O_6$ (Lumsden et al. 2000) or $LiCrSi_2O_6$ (Nenert et al. 2009a), but not for the $C2/c$ structure. A graphical display of the magnetic spin structure is given in Fig. 9. As the bulk magnetic measurements reveal an overall antiferromagnetic character, J_1 dominates J_2, i.e. the ferromagnetic interaction is weak. Despite the same space group symmetry and similar composition, except the Si^{4+} by Ge^{4+} substitution,
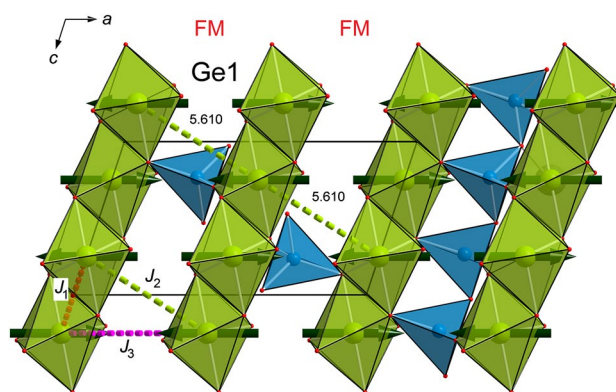

Fig. 9 Collinear magnetic spin structure of $C2/c$ $Li_{0.18}Na_{0.82}FeGe_2O_6$ with **k** = (0 1 0) in a projection onto the **a**–**c** plane at 4 K, as determined from neutron diffraction data, the different inter-chain couplings are again given

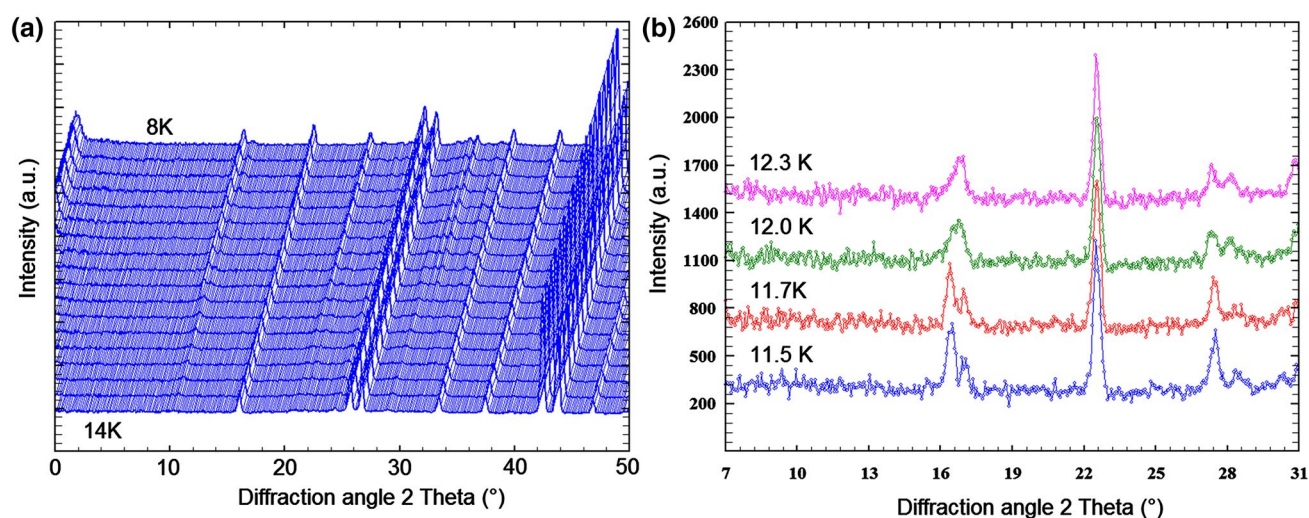**Fig. 10** Neutron diffraction pattern of $Li_{0.12}Na_{0.88}FeGe_2O_6$ in the temperature range 4 to 15 K, the onset of magnetic ordering is clearly seen from the appearance of new Bragg peaks around 14 K. In **b** a more detailed section is depicted to highlight the changes in magnetic Bragg peaks upon change from cycloidal to spin density wave structure

the collinear spin structure of synthetic $NaFeSi_2O_6$ is different and shows a full AFM pattern of ordering of magnetic moments within and between the M1 chains (Baum et al. 2015; Redhammer et al. 2011a).

Similar to $Li_{0.31}Na_{0.69}FeGe_2O_6$, the variation of the magnetic moment M can very well be described by the power law, given in (1). The experimental data, fully consistent with heat capacity and bulk magnetic measurements and with a 3D-model of ordering, are included in Fig. 6, while all the fitting parameters can be found in the ESM Table S5.

Besides the above collinear structure, a spurious incommensurate spin structure is also present in both samples, which is identical with the one, found for sample $Li_{0.12}Na_{0.88}FeGe_2O_6$ (see also ESM Text).

For $Li_{0.12}Na_{0.88}FeGe_2O_6$ first magnetic Bragg peaks appear between 14.0 and 13.7 K and quickly gain intensity (Fig. 10). At 4 K, the powder pattern can be refined as a superimposition of a collinear magnetic structure with **k** = (0 1 0), basis function $[A_x, 0, A_z]$ and an incommensurate one with **k** ~ (0.28, 1, 0.07) and an AFM coupling within the M1 chains. This propagation vector is close to the one of pure end-member $NaFeGe_2O_6$ and yielded good agreement with observed data in pattern matching. It should be noted that a superposition of two magnetic structures is also present in synthetic aegirine $NaFeSi_2O_6$ (Baum et al. 2015; Redhammer et al. 2011a). Graphical representations of the magnetic structures in $Li_{0.12}Na_{0.88}FeGe_2O_6$ are given in Fig. 11.

The collinear structure with **k** = (0 1 0) closely resembles the one of the two samples with $x(Na) = 0.78$ and 0.82. The magnetic moments are aligned along the **a** axis

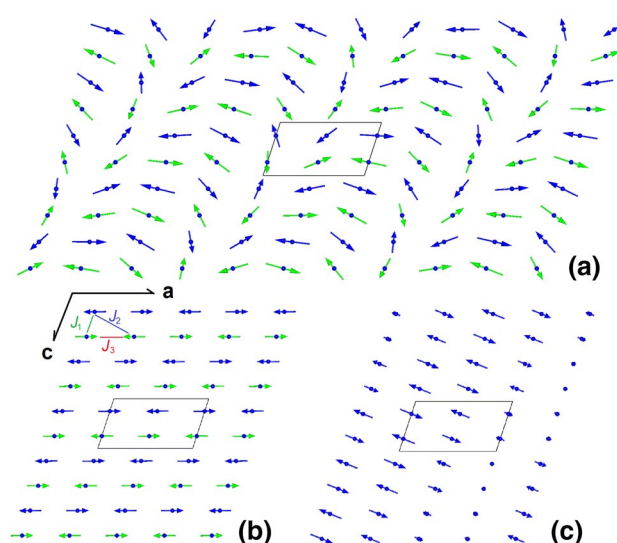**Fig. 11** Schematic drawings of the different magnetic structures in sample $Li_{0.12}Na_{0.88}FeGe_2O_6$ in a projection onto (0 1 0): **a** cycloidal structure at 4 K, **b** simple collinear structure at 4 K and **c** spin density wave structure at 12.5 K

over a wide range of temperatures from 4 K to 12 K. Only very close to the magnetic–paramagnetic phase transition the refinements suggest that spins tend to incline towards the **c** axis; however, intensity data are less accurate here to decide by sure, if this is a real effect. The evolution of the magnetic moment for the collinear magnetic phase is also given in Fig. 7. It shows that the magnetic moment increases quickly in the magnetically ordered phase. However, the size of the moment decreases again below 8 K. This effect is explained as a decrease of the relative fraction

of the collinear magnetic on the expense of the incommensurately modulated structure (see also ESM text). In the critical region of the phase transition (9–12.5 K), the moment data of the collinear structure can be fitted with the given power law, yielding an extrapolated magnetic moment of 3.12(1) µB, an ordering temperature of 12.5 K and a critical exponent of 0.38. The extracted ordering temperature is somewhat lower than observed in C_p measurements; however, up to 14 K there are some weak magnetic Bragg peaks visible, which indicate the presence of the collinear structure.

At 4 K the modulated structure shows a cycloidal magnetic order with the spins aligned within the (0 1 0) plane. Within a cycloidal M1 chain, the spins are close to an antiferromagnetic ordering. Spins in two neighbouring M1 chains, which interact via super–super-exchange along the shortest Fe–Fe inter-chain distance are rotated away from each other by and angle of $\delta \sim 44°$–88°, i.e. they have no parallel spin orientation; however, they are closer to a ferromagnetic than to an antiferromagnetic orientation. In end-member $NaFeGe_2O_6$, the angle between spin orientation in different M1 chains ranges between ~68° and 78°, thus it may be concluded that the spin orientation approaches a FM coupling between neighbouring M1 chains, even if still incommensurately modulated. Generally, the observed magnetic structure is very similar to the one in pure $NaFeGe_2O_6$, and also to the one in natural $NaFeSi_2O_6$, even if the **k**- vector differs (Baum et al. 2015).

Between 11.7 and 12 K, differences in the appearance of the powder patterns are observed (coincidence of doublets, Fig. 10b) and the cycloidal structure transforms to a spin density wave structure. This temperature is in excellent agreement with appearance of a second peak in the low-temperature caloric measurements. The change from cycloidal to SDW structure is associated with a distinct change in the **k** vector as displayed in Fig. 12, which is

additional evidence that a magnetic phase transition occurs at this temperature around 12 K. The magnetic–paramagnetic transition is observed between 14 K and 14.3 K. Again, this temperature is in excellent agreement with the C_p and the results of susceptibility measurements. In the SDW state, the spins are within the (0 1 0) plane forming an angle of ~ 20–30° with the **a** axis having a very similar AFM and FM coupling scheme along J_1 and J_2 as described for the collinear structure, except the rotation of spins away from the **a** axis towards **c**. A SDW to cycloidal structure transition was also described by Baum et al. (2015) for a natural crystal of $NaFeSi_2O_6$, while it is evidently absent in the synthetic end-member composition.

For the $Li_{0.12}Na_{0.88}FeGe_2O_6$ composition, the dataset with small temperature increments allows also to have a detailed look onto the low-temperature variation of lattice parameters. Typically, the pyroxenes show a more or less pronounced magneto-elastic coupling (Redhammer et al. 2013), which also is observable for this composition. While for the a lattice parameter, no change is observed between 4 K and 20 K, these changes are prominent for b and c. Different to what would be expected at such low temperatures, these lattice parameters increase with decreasing temperature. A small plateau with almost constant b and c parameters can be seen in the data between 12 and 13 K, which is the range of stability of the SDW phase, below 12 K, b and c again increase down to ~10 K, below which they stabilize and remain constant (see Fig. 13 and ESM Figure S5). The monoclinic angle increases with decreasing temperature and also stabilizes below 10 K. The AFM ordering and development of the cycloidal structure within the M1 chain thus causes the M1 sites to move further away from each other. Similar behaviours could be found for end-member $NaFeGe_2O_6$, even if the low-temperature variation could not be determined with the present richness of detail.
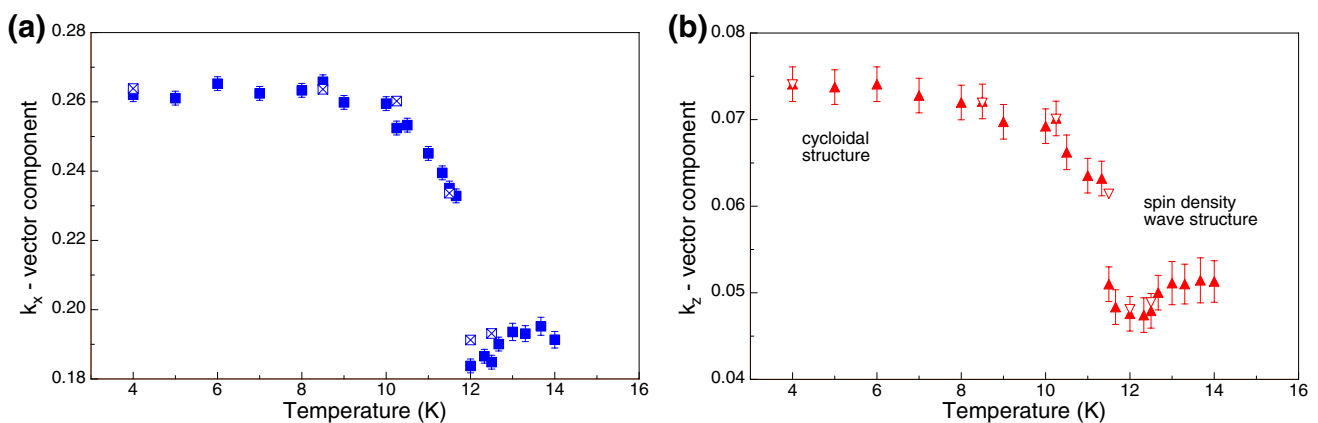

Fig. 12 Variation of the **k** vector components with temperature for the incommensurably modulated magnetic structures in sample $Li_{0.12}Na_{0.88}FeGe_2O_6$, the closed and open symbols represent the short- and long-time measurements, respectively

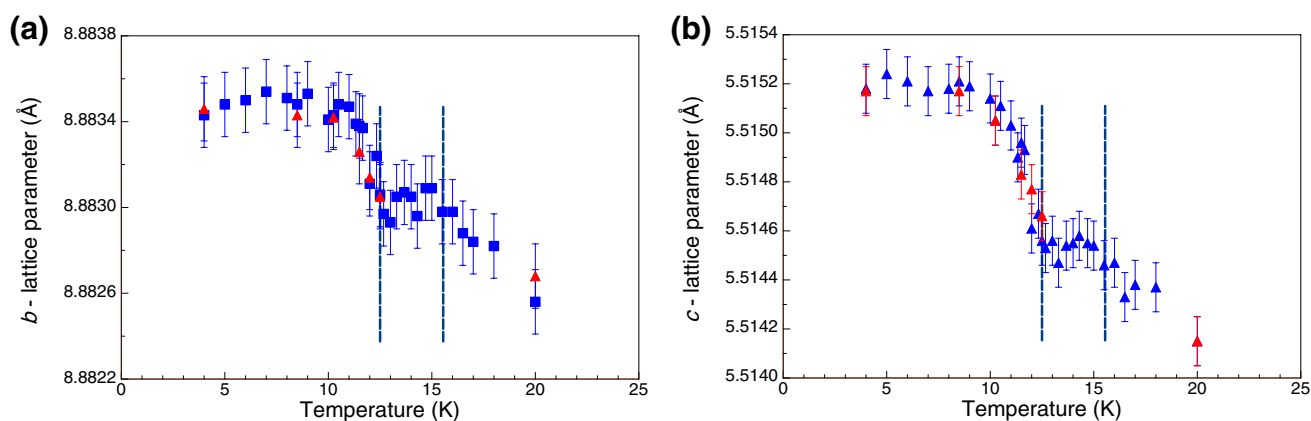**Fig. 13** Variation of lattice parameters of $Li_{0.12}Na_{0.88}FeGe_2O_6$ with temperature (also compare ESM Figure S6), *blue squares* correspond to the short, *red triangles* to the long-time measurements, the *dashed lines* mark the stability of the spin density wave structure

Summary and conclusion

The substitution of Li by Na along the $Li_{1-x}Na_xFeGe_2O_6$ solid solution series entails a change in the crystal structure from $P2_1/c$ to $C2/c$ around x(Na) ~0.75 at 4 K. Samples between x(Na) = 0.0 and 0.72 show a magnetic spin structure which can be described with $\mathbf{k} = (\frac{1}{2}, 0\ 0)$, in agreement with the structures described by Redhammer et al. (2009) and Drokina et al. (2015). The reduction of the Néel temperature from pure $LiFeGe_2O_6$ to $Li_{0.25}Na_{0.75}FeGe_2O_6$ by ~7 K may be related to an increasing distance between the M1 chains from 5.546(1) to 5.614(1) Å and 5.423(1) to 5.587(1) Å in $LiFeGe_2O_6$ and $Li_{0.25}Na_{0.75}Ge_2O_6$ involving the GeA- and GeB-chains, respectively. The distances of Fe–Fe atoms within the chain are not changing that much. Also, the reduction of the effective magnetic moment of Fe^{3+}, which can be interpreted as increased magnetic frustration, can be seen in the light of these structural alterations. As the distance between chains increases with increasing x(Na), the interaction between the chains, which is ferromagnetic, is likely weakened and/or frustration is enhanced. This agrees with the increasing paramagnetic Curie temperature, indicating increasing overall antiferromagnetic correlation and the decreasing magnetic moments, indicating more frustration. In the vicinity of the structural phase transition at x(Na) ~ 0.75, the magnetic structure changes to an incommensurately modulated one, though the crystal structure is still $P2_1/c$. This is a somewhat unexpected result, as it was assumed as a working hypothesis, that modulated structures are restricted to $C2/c$ pyroxenes.

For samples with $C2/c$ symmetry, the magnetic structures can be described as a coexistence of a simple commensurate and a complex incommensurately modulated spin structure. For x(Na) = 0.78 and 0.82 the dominating magnetic structure is commensurate with $\mathbf{k} = (0\ 1\ 0)$. However, small admixtures of the incommensurately modulated second magnetic structure also are present. Thus, the magnetic structure of the $C2/c$ samples is a superimposition of both a collinear and a modulated structure. For x(Na) = 0.78 and 0.82 the collinear structure is dominating but with increasing x(Na) the modulated structure becomes prevailing as is shown for x(Na) = 0.88. Here we also could show a magnetic transition from a cycloidal to a spin density wave magnetic structure. This explains the presence of two peaks in the low-temperature caloric data for these compounds.

A x – T phase diagram similar to the $Li_{1-x}NaFeGe_2O_6$ system might also hold true for the silicate system: natural samples of aegirine $NaFeSi_2O_6$—still being modulated—show a different spin structure to synthetic end-member $NaFeSi_2O_6$, which most probably is induced by small substitutional effects (Baum et al. 2015). More work, including investigation of effects of coupled $CaMgSi_2O_6$–$NaFeSi_2O_6$ substitutions, both in the silicate as well as in the germanate system may help to shed additional light onto the complex ordering schemes within the pyroxene group in general, and onto the (Na,Li) $Fe(Si,Ge)_2O_6$ subsystem in special.

From the results, reported here, it is obvious, that even small chemical substitutions and structural alterations change the magnetic ground states distinctly; nevertheless, there is no simple structural parameter which entirely controls the formation of a given magnetic structure. Simple crystal-chemical relations cannot fully explain the complex ordering pattern within the $Li_{1-x}Na_xFeGe_2O_6$ solid solution series. So, for interpreting magneto-structural correlations, it is essential to calculate the single exchange pathways. For example, different magnetic couplings paths within the M1-chains, not

only along J_1, but also between more distant Fe–Fe cations, may also be responsible for cycloidal ordering and transition to SDW, so the calculations of coupling constants is indeed an essential need for a more in-detailed explanation of these systems. Estimating strengths and signs of exchange couplings based on structural details only can at most give rough estimations. Basis for any theoretical calculations of exchange pathways and their strengths are high-quality low-temperature structural data, which are now available. However, the computation of exchange pathways in Fe-compounds, e.g. within DFT, is still a major problem because of orbital degrees of freedom, different correlation strengths for the d-orbitals, etc. We, thus, have not considered such an analysis for the present study.

References

Ackermann M, Andersen L, Lorenz T, Bohaty L, Becker P (2015) Anisotropy study of multiferroicity in the pyroxene NaFeGe$_2$O$_6$. New J Phys 17

Alvaro M, Camara F, Domeneghetti MC, Nestola F, Tazzoli V (2011) HT $P2_1/c$-$C2/c$ phase transition and kinetics of Fe^2+-Mg order-disorder of an Fe-poor pigeonite: implications for the cooling history of ureilites. Contrib Miner Petrol 162(3):599–613

Aroyo MI, Kirov A, Capillas C, Perez-Mato JM, Wondratschek H (2006a) Bilbao crystallographic server. II. Representations of crystallographic point groups and space groups. Acta Crystallogr A Found Adv 62:115–128

Aroyo MI, Perez-Mato JM, Capillas C, Kroumova E, Ivantchev S, Madariaga G, Kirov A, Wondratschek H (2006b) Bilbao crystallographic server: I. Databases and crystallographic computing programs. Zeitschrift Fur Kristallographie 221(1):15–27

Aroyo MI, Perez-Mato JM, Orobengoa D, Tasci E, de la Flor G, Kirov A (2011) Crystallography online: Bilbao Crystallographic Server. Bul Chem Commun 43(2):183–197

Baum M, Komarek AC, Holbein S, Fernández-Díaz MT, André G, Hiess A, Sidis Y, Steffens P, Becker P, Bohatý L, Braden M (2015) Magnetic structure and multiferroic coupling in pyroxene NaFeSi$_2$O$_6$. Phys Rev B 91(21):214415

Blundell SJ, Steer CA, Pratt FL, Marshall IM, Hayes W, Ward RCC (2003) Detection of magnetic order in the S = 1D chain compound LiVGe$_2$O$_6$ using implanted spin-polarized muons. Phys Rev B 67(22):224411

Braden M, Wilkendorf G, Lorenzana J, Ain M, McIntyre GJ, Behruzi M, Heger G, Dhalenne G, Revcolevschi A (1996) Structural analysis of CuGeO$_3$: relation between nuclear structure and magnetic interaction. Phys Rev B 54(2):1105–1116

Camara F, Nestola F, Angel RJ, Ohashi H (2009) Spontaneous strain variations through the low-temperature displacive phase transition of LiGaSi$_2$O$_6$ clinopyroxene. Eur J Miner 21(3):599–614

Cheng J, Tian W, Zhou J, Lynch VM, Steinfink H, Manthiram A, May AF, Garlea VO, Neuefeind JC, Yan J (2013) Crystal and magnetic structures and physical properties of a new pyroxene NaMnGe$_2$O$_6$ synthesized under high pressure. J Am Chem Soc 135(7):2776–2786

Dong S, Liu JM, Cheong SW, Ren ZF (2015) Multiferroic materials and magnetoelectric physics: symmetry, entanglement, excitation, and topology. Adv Phys 64(5–6):519–626

Drokina TV, Petrakovskii GA, Keller L, Schefer J, Balaev AD, Kartashev AV, Ivanov DA (2011) Modulated magnetic structure in quasi-one-dimensional clinopyroxene NaFeGe$_2$O$_6$. J Exp Theor Phys 112(1):121–126

Drokina TV, Petrakoyskii GA, Molokeev MS, Misyul SV, Bondarev VS, Velikanov DA, Frontzek M, Schefer J (2015) Crystal and magnetic structures, phase transitions in quasi-one-dimensional pyroxenes Na$_{0.5}$Li$_{0.5}$FeGe$_2$O$_6$. J Magn Magn Mater 385:243–249

Drokina TV, Petrakovskii GA, Molokeev MS, Bondarev VS, Velikanov DA (2016) Synthesis and study of structural, thermodynamic, and magnetic properties of Na$_x$Li$_{1-x}$FeGe$_2$O$_6$ (x = 0.1–0.9) compounds. Phys Solid State 58(7):1361–1370

Fiebig M, Lottermoser T, Meier D, Trassin M (2016) The evolution of multiferroics. Nature Reviews Materials, 1(8)

Fisher ME (1962) Relation between the specific heat and susceptibility of an antiferromagnet. Phil Mag 7(82):1731–1743

Furukawa S, Sato M, Onoda S (2010) chiral order and electromagnetic dynamics in one-dimensional multiferroic cuprates. Physical Review Letters, 105(25)

Geertsma W, Khomskii D (1996) Influence of side groups on 90 degrees superexchange: a modification of the Goodenough-Kanamori-Anderson rules. Phys Rev B 54(5):3011–3014

Hoelzel M, Senyshyn A, Juenke N, Boysen H, Schmahl W, Fuess H (2012) High-resolution neutron powder diffractometer SPODI at research reactor FRM II. Nucl Instrum Methods Phys Res, Sect A 667:32–37

Janson O, Nenert G, Isobe M, Skourski Y, Ueda Y, Rosner H, Tsirlin AA (2014) Magnetic pyroxenes LiCrGe$_2$O$_6$ and LiCrSi$_2$O$_6$: Dimensionality crossover in a nonfrustrated S = 3/2 Heisenberg model. Physical Review B, 90(21)

Jodlauk S, Becker P, Mydosh JA, Khomskii DI, Lorenz T, Streltsov SV, Hezel DC, Bohaty L (2007) Pyroxenes: a new class of multiferroics. Journal of Physics-Condensed Matter, 19(43)

Khomskii DI (2006) Multiferroics: different ways to combine magnetism and ferroelectricity. J Magn Magn Mater 306(1):1–8

Khomskii DI (2014) Ferroelectrics, magnetoelectrics, and multiferroics. Transition Metal Compounds, 269–309

Kim I, Jeon BG, Patil D, Patil S, Nenert G, Kim KH (2012) Observation of multiferroic properties in pyroxene NaFeGe$_2$O$_6$. Journal of Physics-Condensed Matter, 24(30)

Lebernegg S, Schmitt M, Tsirlin AA, Janson O, Rosner H (2013a) Magnetism of CuX$_2$ frustrated chains (X = F, Cl, Br): Role of covalency. Physi Rev B 87(15)

Lebernegg S, Tsirlin AA, Janson O, Rosner H (2013b) Two energy scales of spin dimers in clinoclase Cu$_3$(AsO$_4$)(OH)$_3$. Phys Rev B 87(23)

Lebernegg S, Tsirlin AA, Janson O, Rosner H (2014) Nearly compensated exchange in the dimer compound callaghanite Cu$_2$Mg$_2$(CO$_3$)(OH)$_6$ · 2H$_2$O. Phys Rev B 89(16)

Lebernegg S, Tsirlin AA, Janson O, Redhammer GJ, Rosner H (2016) Interplay of magnetic sublattices in langite $Cu_4(OH)_6SO_4 \cdot 2H_2O$. New J Phys 18

Lebernegg S, Janson O, Rousochatzakis I, Nishimoto S, Rosner H, Tsirlin AA (2017) Frustrated spin chain physics near the Majumdar-Ghosh point in szenicsite $Cu_3(MoO_4)(OH)_4$. Phys Rev B 95(3):035145

Lumsden MD, Granroth GE, Mandrus D, Nagler SE, Thompson JR, Castellan JP, Gaulin BD (2000) Long-range antiferromagnetic order in the S = 1 chain compound $LiVGe_2O_6$. Phys Rev B 62(14):R9244–R9247

Nenert G, Isobe M, Ritter C, Isnard O, Vasiliev AN, Ueda Y (2009a) Magnetic and crystal structures of the magnetoelectric pyroxene $LiCrSi_2O_6$. Phys Rev B 79(6)

Nenert G, Ritter C, Isobe M, Isnard O, Vasiliev AN, Ueda Y (2009b) Magnetic and crystal structures of the one-dimensional ferromagnetic chain pyroxene $NaCrGe_2O_6$. Phys Rev B 80(2)

Nenert G, Isobe M, Kim I, Ritter C, Colin CV, Vasiliev AN, Kim KH, Ueda Y (2010a) Interplay between low dimensionality and magnetic frustration in the magnetoelectric pyroxenes $LiCrX_2O_6$ (X = Ge, Si). Phys Rev B 82(2)

Nenert G, Kim I, Isobe M, Ritter C, Vasiliev AN, Kim KH, Ueda Y (2010b) Magnetic and magnetoelectric study of the pyroxene $NaCrSi_2O_6$. Physical Review B, 81(18)

Nestola F, Redhammer GJ, Pamato MG, Secco L, Dal Negro A (2009) High-pressure phase transformation in $LiFeGe_2O_6$ pyroxene. Am Miner 94(4):616–621

Park S, Choi YJ, Zhang CL, Cheong SW (2007) Ferroelectricity in an S = 1/2 Chain Cuprate. Phys Rev Lett 98(5):057601

Perez-Mato JM, Gallego SV, Tasci ES, Elcoro L, de la Flor G, Aroyo MI (2015) Symmetry-based computational tools for magnetic crystallography. In D.R. Clarke, Ed. Annu Rev Mater Res 45(45):217–248

Redhammer GJ, Roth G (2004a) Structural changes upon the temperature dependent C2/c −>$P2_1$/c phase transition in $LiMe^{3+}Si_2O_6$ clinopyroxenes, Me = Cr, Ga, Fe, V, Sc and In. Zeitschrift Fur Kristallographie 219(10):585–605

Redhammer GJ, Roth G (2004b) Structural variation and crystal chemistry of $LiMe^{3+}Si_2O_6$ clinopyroxenes Me^{3+} = Al, Ga, Cr, V, Fe, Sc and In. Zeitschrift Fur Kristallographie 219(5):278–294

Redhammer GJ, Tippelt G (2014) Pyroxene-type compounds $NaM^{3+}Ge_2O_6$, with M = Ga, Mn, Sc and In. Acta Crystallographica Section C-Structural Chemistry, 70, 852

Redhammer GJ, Tippelt G (2016) The $(Na,Li)FeGe_2O_6$ clinopyroxene-type series: a temperature-dependent single-crystal X-ray diffraction and ^{57}Fe Mossbauer spectroscopic study. Phys Chem Miner 43(1):1–22

Redhammer GJ, Roth G, Paulus W, Andre G, Lottermoser W, Amthauer G, Treutmann W, Koppelhuber-Bitschnau B (2001) The crystal and magnetic structure of Li-aegirine $LiFe^{3+}Si_2O_6$: a temperature-dependent study. Phys Chem Miner 28(5):337–346

Redhammer GJ, Roth G, Treutmann W, Paulus W, Andre G, Pietzonka C, Amthauer G (2008) Magnetic ordering and spin structure in Ca-bearing clinopyroxenes $CaM^{2+}(Si, Ge)_2O_6$, M = Fe, Ni Co, Mn. J Solid State Chem 181(11):3163–3176

Redhammer GJ, Roth G, Treutmann W, Hoelzel M, Paulus W, Andre G, Pietzonka C, Amthauer G (2009) The magnetic structure of clinopyroxene-type $LiFeGe_2O_6$ and revised data on multiferroic $LiFeSi_2O_6$. J Solid State Chem 182(9):2374–2384

Redhammer GJ, Camara F, Alvaro M, Nestola F, Tippelt G, Prinz S, Simons J, Roth G, Amthauer G (2010a) Thermal expansion and high-temperature $P2_1$/c-C2/c phase transition in clinopyroxene-type $LiFeGe_2O_6$ and comparison to $NaFe(Si,Ge)_2O_6$. Phys Chem Miner 37(10):685–704

Redhammer GJ, Senyshyn A, Tippelt G, Pietzonka C, Roth G, Amthauer G (2010b) Magnetic and nuclear structure and thermal expansion of orthorhombic and monoclinic polymorphs of $CoGeO_3$ pyroxene. Phys Chem Miner 37(5):311–332

Redhammer GJ, Senyshyn A, Meven M, Roth G, Prinz S, Pachler A, Tippelt G, Pietzonka C, Treutmann W, Hoelzel M, Pedersen B, Amthauer G (2011a) Nuclear and incommensurate magnetic structure of $NaFeGe_2O_6$ between 5 K and 298 K and new data on multiferroic $NaFeSi_2O_6$. Phys Chem Miner 38(2):139–157

Redhammer GJ, Senyshyn A, Tippelt G, Roth G (2011b) Magnetic spin structure of pyroxene-type $MnGeO_3$. Journal of Physics-Condensed Matter, 23(25)

Redhammer GJ, Senyshyn A, Tippelt G, Pietzonka C, Treutmann W, Roth G, Amthauer G (2012) Magnetic and low-temperature structural behavior of clinopyroxene-type $FeGeO_3$: a neutron diffraction, magnetic susceptibility, and ^{57}Fe Mossbauer study. Am Miner 97(4):694–706

Redhammer GJ, Roth G, Senyshyn A, Tippelt G, Pietzonka C (2013) Crystal and magnetic spin structure of Germanium-Hedenbergite, $CaFeGe_2O_6$, and a comparison with other magnetic/magneto-electric/multiferroic pyroxenes. Zeitschrift Fur Kristallographie 228(3):140–150

Redhammer GJ, Senyshyn A, Tippelt G, Prinz S, Roth G (2015) Structural and magnetic phase transitions in the synthetic clinopyroxene $LiCrGe_2O_6$: a neutron diffraction study between 0.5 and 1473 K. Phys Chem Miner 42(6):491–507

Rodríguez-Carvajal J (2001) Recent developments of the program FULLPROF, http://www.ill.eu/sites/fullprof/. Commission on Powder Diffraction (IUCr), Newsletter 26

Ruiz E, Alemany P, Alvarez S, Cano J (1997) Structural modeling and magneto-structural correlations for hydroxo-bridged copper(II) binuclear complexes. Inorg Chem 36(17):3683–3688

Spaldin NA, Fiebig M (2005) The renaissance of magnetoelectric multiferroics. Science 309(5733):391–392

Streltsov SV, Khomskii DI (2008) Electronic structure and magnetic properties of pyroxenes (Li,Na)TM$(Si,Ge)_2O_6$: Low-dimensional magnets with 90 degrees bonds. Phys Rev B 77(6)

Tokura Y (2006) Multiferroics as quantum electromagnets. Science, 312(5779), 1481

Tribaudino M, Nestola F, Camara F, Domeneghetti MC (2002) The high-temperature $P2_1$/c - C2/c phase transition in Fe-free pyroxene $(Ca_{0.15}Mg_{1.85}Si_2O_6)$: structural and thermodynamic behavior. Am Miner 87(5–6):648–657

Tribaudino M, Nestola F, Meneghini C, Bromiley GD (2003) The high-temperature $P2_1$/c - C2/c phase transition in Fe-free Ca-rich $P2_1$/c clinopyroxenes. Phys Chem Miner 30(9):527–535